

# High-throughput single-cell density measurements enable dynamic profiling of immune cell and drug response from patient samples

Received: 2 October 2023

Accepted: 16 April 2025

Published online: 20 May 2025

 Check for updates

Weida Wu <sup>1,2</sup>, Sarah H. Ishamuddin<sup>1</sup>, Thomas W. Quinn <sup>3,4</sup>, Smitha Yerrum<sup>3,4</sup>, Ye Zhang <sup>1</sup>, Lydie L. Debaize<sup>5</sup>, Pei-Lun Kao<sup>3,4</sup>, Sarah Marie Duquette<sup>1,2</sup>, Mark A. Murakami <sup>5</sup>, Morvarid Mohseni<sup>6</sup>, Kin-Hoe Chow<sup>3,4</sup>, Teemu P. Miettinen <sup>1</sup>, Keith L. Ligon <sup>3,4,7,8,9</sup>  & Scott R. Manalis <sup>1,2,7,10</sup> 

Cell density, the ratio of cell mass to volume, is an indicator of molecular crowding and a fundamental determinant of cell state and function. However, existing density measurements lack the precision or throughput to quantify subtle differences in cell states, particularly in primary samples. Here we present an approach for measuring the density of 30,000 single cells per hour by integrating fluorescence exclusion microscopy with a suspended microchannel resonator. This approach achieves a precision of 0.03% ( $0.0003 \text{ g ml}^{-1}$ ) for cells larger than  $12 \mu\text{m}$  in diameter. In human lymphocytes, we discover that cell density and its variation decrease as cells transition from quiescence to a proliferative state, suggesting that the level of molecular crowding decreases and becomes more regulated upon entry into the cell cycle. Using a pancreatic cancer patient-derived xenograft model, we find that the ex vivo density response of primary tumour cells to drug treatment can predict the in vivo tumour growth response. Our method reveals unexpected behaviour in molecular crowding during cell state transitions and suggests density as a biomarker for functional precision medicine.

Cell density is determined by the cell's dry mass composition and the fraction of cell volume occupied by water, which reflects its molecular crowding level. Although cell mass and volume can vary up to 50% in proliferating cells, cell density is tightly regulated to maintain an optimal level of molecular crowding<sup>1–3</sup>. Environmental cues such as nutrient depletion and changes in osmolarity are known to alter molecular crowding, which impacts cellular biochemistry by altering the diffusion rate and protein conformation<sup>1,4,5</sup>. The coupling between crowding level and cell physiology makes cell density a key proxy for characterizing fundamental cellular processes such as proliferation, apoptosis, metabolic shifts and differentiation<sup>1,3</sup>, indicating its potential as a biomarker for cellular fitness and drug response. Studies on

single-cell organisms such as bacteria and yeast have reported that molecular crowding levels substantially change during cell state transitions between proliferation and dormancy, and density is thought to acutely reflect these transitions<sup>5–8</sup>. Whether such connections between density and proliferation exist in primary mammalian cells remains unclear, in part due to limitations in existing methods.

A major challenge for measuring cell density is achieving high sampling throughput together with high precision. Traditional gradient centrifugation methods assess cell densities on a populational level, but are slow and require a large sample size, which limits their use for studying transient biological processes. Single-cell measurements reveal the heterogeneity of cell density within a population, providing insight into

A full list of affiliations appears at the end of the paper.  e-mail: [keith\\_ligon@dfci.harvard.edu](mailto:keith_ligon@dfci.harvard.edu); [srm@mit.edu](mailto:srm@mit.edu)

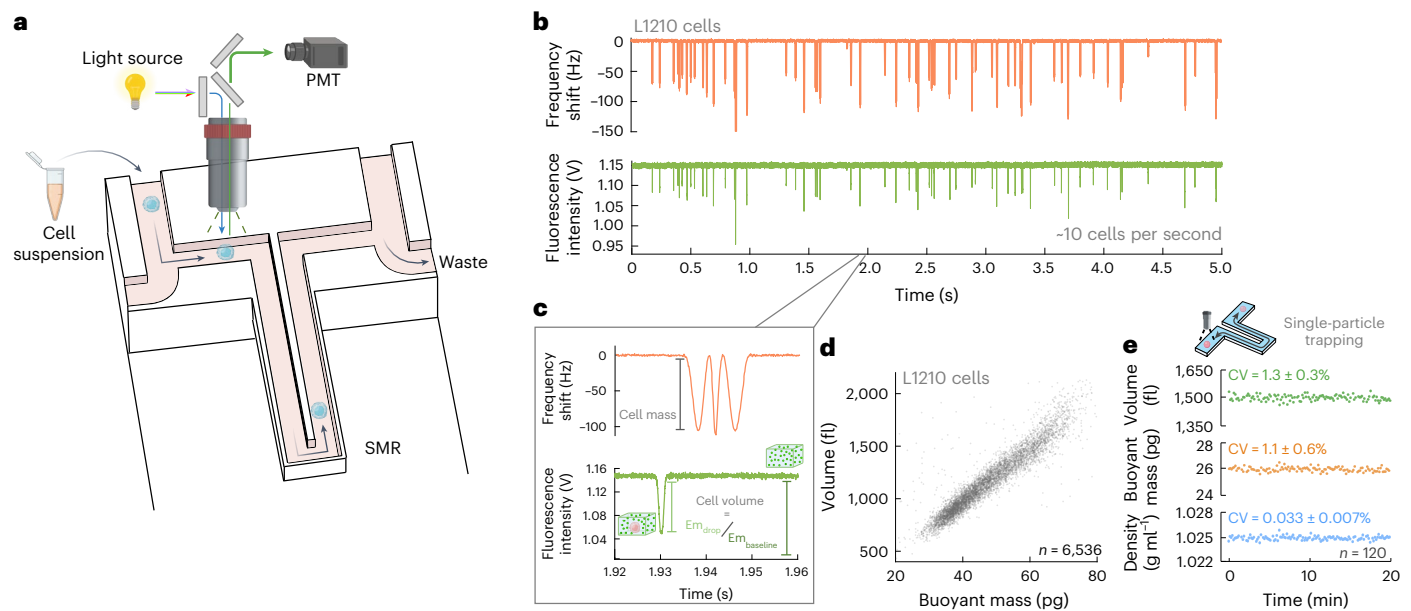


**Fig. 1 | FxSMR enables high-throughput and high-precision single-cell density measurements.** **a**, A schematic showing the system design. A fluorescence detection set up is positioned above the SMR microfluidic chip; the green shaded area indicates the fluorescence detection region and black arrows indicate the flow direction of single cells (blue). **b**, Raw signals from SMR (orange) and the photomultiplier tube (green) when measuring L1210 cells. Each peak indicates the passing of a single cell. **c**, A zoomed-in image of **b**, highlighting the shape of SMR and PMT signals for a single cell, and the calculation of cell volume from the

in fluorescence signal ( $Em_{\text{drop}}$ ) from the fluorescence baseline ( $Em_{\text{baseline}}$ ). **d**, A scatter plot of cell mass versus volume for a population of L1210 cells as measured in ~20 min.  $n$  refers to the number of individual cells. **e**, Representative plots of volume, mass and density of a single hydrogel microparticle that was measured repeatedly using fluidic trapping; The measurement precision (CV) is reported for each metric (mean  $\pm$  s.d. for 5 independently trapped particles).  $n$  refers to the number of repeat measurements for the individual particle shown in the plots. Figure created with [BioRender.com](#).

density regulation. Magnetic levitation methods determine the density of single cells by balancing the cell's gravity and the buoyancy exerted by a paramagnetic medium<sup>9,10</sup>. Methods detecting dry-mass density (dry mass over total volume), such as quantitative-phase microscopy or Raman imaging coupled with cell volume measurements, provide alternative density measurements<sup>11–16</sup>. Although these methods provide subcellular resolution and single-cell tracking, their applications are limited by low throughput, where a typical experiment includes tens to hundreds of single cells when measuring cell density. The suspended microchannel resonator (SMR) is a microfluidic mass sensor that has been used to measure single-cell density by measuring the buoyant mass of a cell in two types of fluids with different densities<sup>17–20</sup>. However, the throughput of this approach is also limited to a few hundred cells per experiment because it requires cells to be sequentially measured in two types of fluids.

SMR and quantitative-phase microscopy devices have already achieved a throughput of tens-to-hundreds of thousands of cells per experiment<sup>21–23</sup>. With a streamlined volume-sensing unit, the same throughput could be achieved for measuring cell density. Fluorescence exclusion microscopy (fxm) provides a volume measurement compatible with existing SMR devices. Fxm measures the exclusion of fluorescence intensity induced by single cells that are suspended in a highly fluorescent media with cell-impermeable dye molecules. This method has been adapted to measure single-cell volumes of various model systems including bacteria, yeast and mammalian cells<sup>24,25</sup>.

Here, we present a fluorescence exclusion-coupled SMR (fxSMR) platform that simultaneously measures single-cell buoyant mass and volume, which allows us to profile cell density with a throughput of over 30,000 cells per hour and a precision of 0.03% ( $0.0003 \text{ g ml}^{-1}$ ) for cells larger than  $12 \mu\text{m}$  in diameter. We show three advances that are enabled by our high throughput and precision. We identify unexpected density heterogeneity, reveal molecular crowding associated changes during cell state transition and validate density as a new biomarker of drug response.

## Results

### Platform design and characterization

To couple single-cell mass and volume measurements, our system is composed of an SMR cantilever with microfluidic inlets for receiving a stream of single cells and a fluorescence microscopy set up positioned at the entry of the resonator chamber (Fig. 1a). The fluorescence level emitted from the detection region is continuously monitored by a photomultiplier tube (PMT). To achieve the fluorescence exclusion volume measurements, cells are suspended in a fluorescent media that contains cell-impermeable dye-conjugated dextran. When there is no cell present at the detection region, the PMT detects a high fluorescence baseline from the media. As the cell passes through, the fluorescence level decreases proportionally to the volume of the cell. The raw volume signal is computed by taking the ratio of the change in fluorescence level to the baseline height (Fig. 1b,c).

Cells flow through the SMR after volume measurement and the buoyant mass signal can be resolved from the change in SMR resonance frequency<sup>17,26</sup>. Cell density, or buoyant density, is then computed by

$$\rho_{\text{cell}} = \frac{\text{buoyant mass}}{\text{volume}} + \rho_{\text{fluid}} \quad (1)$$

We profiled a mouse lymphocytic leukaemia cell line, L1210, and simultaneously obtained single-cell buoyant mass and volume readouts with a throughput of >30,000 cells per hour (Fig. 1b,d).

We then characterized the accuracy of the volume and buoyant mass measurements. Using five cell lines with median cell diameters ranging from  $12.6$  to  $21.0 \mu\text{m}$ , we found a linear correlation (Pearson correlation coefficient  $R^2 = 0.9986$ ) between cell volume measured by Fxm and ground-truth volumes determined by a Coulter counter (Supplementary Fig. 1a,b). Similarly, using five populations of mono-dispersed polystyrene beads ranging from  $5$  to  $9 \mu\text{m}$  in diameter, we found a linear correlation (Pearson correlation coefficient  $R^2 = 0.9998$ )

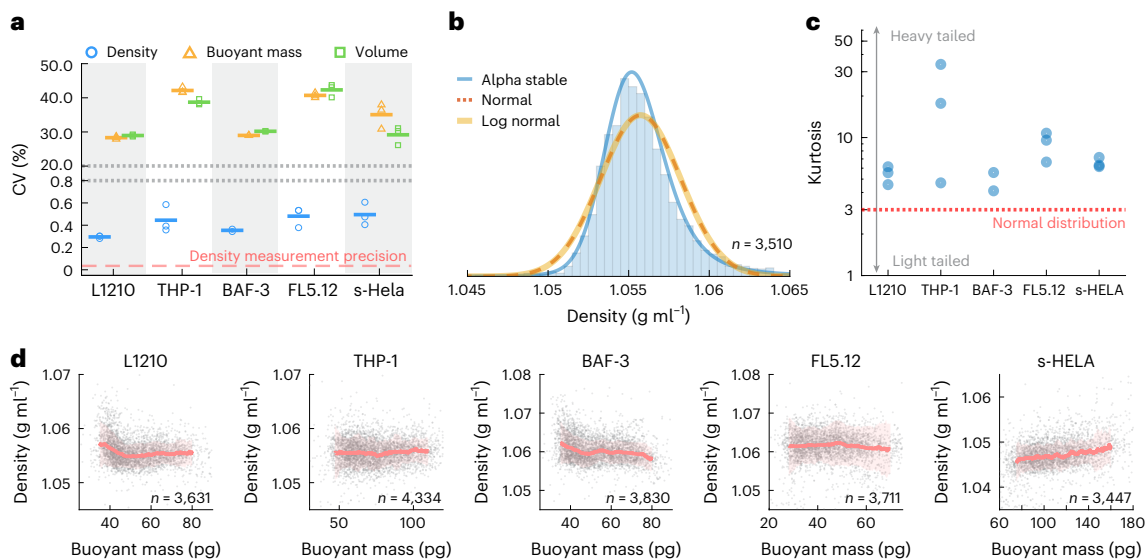


**Fig. 2 | Single-cell densities have a tight and non-Gaussian distribution.** **a**, The CV of density, buoyant mass and volume for five cell lines. Each marker represents an independent replicate; the short horizontal bars denote mean of density, buoyant mass and volume in the corresponding colour; the dashed red line denotes the system precision of density measurements. **b**, The density distribution of L1210 cells with lines indicating normal (dotted red), log-normal (orange) and stable (blue) distribution fitting.  $n$  refers to the number of

individual cells. **c**, The kurtosis factor of the five cell lines. Each marker represents an independent replicate. **d**, Representative scatter plot of mass versus density for the five cell lines. The red lines and shaded red areas indicate median  $\pm$  s.d. of cell density in a moving filter along the buoyant mass axis. The grey points depict single cells and  $n$  values refer to the number of individual cells. For **a**, **c** and **d**,  $n = 3$  biological replicates for L1210, THP-1, FL5.12 and s-Hela and  $n = 2$  biological replicates for BAF-3.

between the SMR frequency shifts and the expected buoyant mass calculated from bead sizes (Supplementary Fig. 1c,d).

To characterize measurement precision, we repeatedly measured the buoyant mass, volume and density of single hydrogel particles in the range of 12.5–14.4  $\mu\text{m}$  in diameter and naive B cells in the range of 6.7–7.0  $\mu\text{m}$  in diameter (Supplementary Fig. 1e–g). The average coefficients of variation (CVs) from five independently trapped hydrogel particles were 1.3% (volume), 1.1% (buoyant mass) and 0.03% (density) (Fig. 1e and Supplementary Fig. 1e–g). We found that density measurement CV increased to 0.30% for naive B cells due to the size-dependent precision of our volume measurement (Supplementary Fig. 1f,g and Supplementary Note 1). These results demonstrate that the fxSMR platform achieves a 10–100-fold increase in throughput over previous approaches<sup>9–17,20</sup> while maintaining high accuracy and precision.

### Density variation in proliferating mammalian cells

Next, we sought to examine the heterogeneity of single-cell densities within a population, as enabled by the high-throughput nature of our density measurement. Most biological features with homeostatic regulatory mechanisms tend to exhibit a Gaussian distribution<sup>27</sup>. An exception from this rule is the distribution of cell size, which follows a log-normal distribution due to cell growth being exponential<sup>28,29</sup>. A deviation from the Gaussian distribution would suggest the existence of a more complex control mechanism compared with a simple negative feedback mechanism.

We started by characterizing five suspension-grown mammalian cell lines, L1210, THP-1, BaF-3, FL5.12 and s-Hela. For statistical analysis, we gated on the viable cell population using a viability marker (Supplementary Note 2). The CV of cell density in all five models are below 0.6%, while the CV of mass and volume are considerably larger, with a range between 20% and 30% (Fig. 2a). This is consistent with previous reports on density heterogeneity in mammalian cells<sup>1,18</sup>. Since the density CV is more than tenfold higher than our measurement precision (Figs. 1e and 2a), our approach is well suited to examine the shape of density distributions. Unexpectedly, cell densities in all five cell lines did not fit to a

normal distribution (Fig. 2b and Supplementary Fig. 2a). We also found that a log-normal distribution did not fit well with cell density when compared with mass and volume (Supplementary Fig. 2a–c). The density distributions were asymmetric and better fitted by a distribution model (stable distribution) that accounts for the ‘heavy-tailed-ness’ of the distribution (Fig. 2b and Supplementary Fig. 2a,d). Consistent with this, the kurtosis factors of the density distributions were all higher than 3, whereas a normal distribution has kurtosis of 3 (Fig. 2c). Moreover, since the hydrogel particle density measurements displayed normal distributions (Supplementary Fig. 2e), the higher kurtosis in cells is biological rather than a reflection of measurement bias.

We next considered the cell cycle as a potential source of density variation. We used cell size as a proxy for cell cycle progression because they are tightly correlated<sup>28,30–33</sup>. From the five suspension cell line models, we did not observe any systematic correlation between cell mass and density, although individual cell lines show distinct features of cell cycle-dependent density (Fig. 2d and Supplementary Fig. 3). These results confirm that for proliferating suspension-grown mammalian cells, cell cycle progression (within interphase) does not introduce changes in cell density that would be shared between cell lines. Given prior evidence that cellular dry mass density does not vary during the cell cycle<sup>34</sup>, the molecular crowding level appears largely independent of the cell cycle stage within interphase. Furthermore, in every cell line, both light (<median buoyant mass) and heavy cells (>median buoyant mass) display kurtosis higher than 3, suggesting the heavy-tailed distributions are not due to a particular cell cycle stage (Supplementary Fig. 2f).

### Density changes during cytotoxic T cell activation

Our results indicate that cell density does not systematically change when cells are cycling in interphase, but previous studies have revealed that cell cycle exit due to cell senescence can alter density<sup>35</sup>. Similarly, in single-cell organisms, cells can enter a quiescence state where the cells display higher molecular crowding (that is, higher density) and smaller cell size<sup>5–7</sup>. We therefore examined whether density homeostasis is specific to cycling cells (Fig. 3a). To study this, we focused on models where we can compare cell density in quiescence and proliferative states.

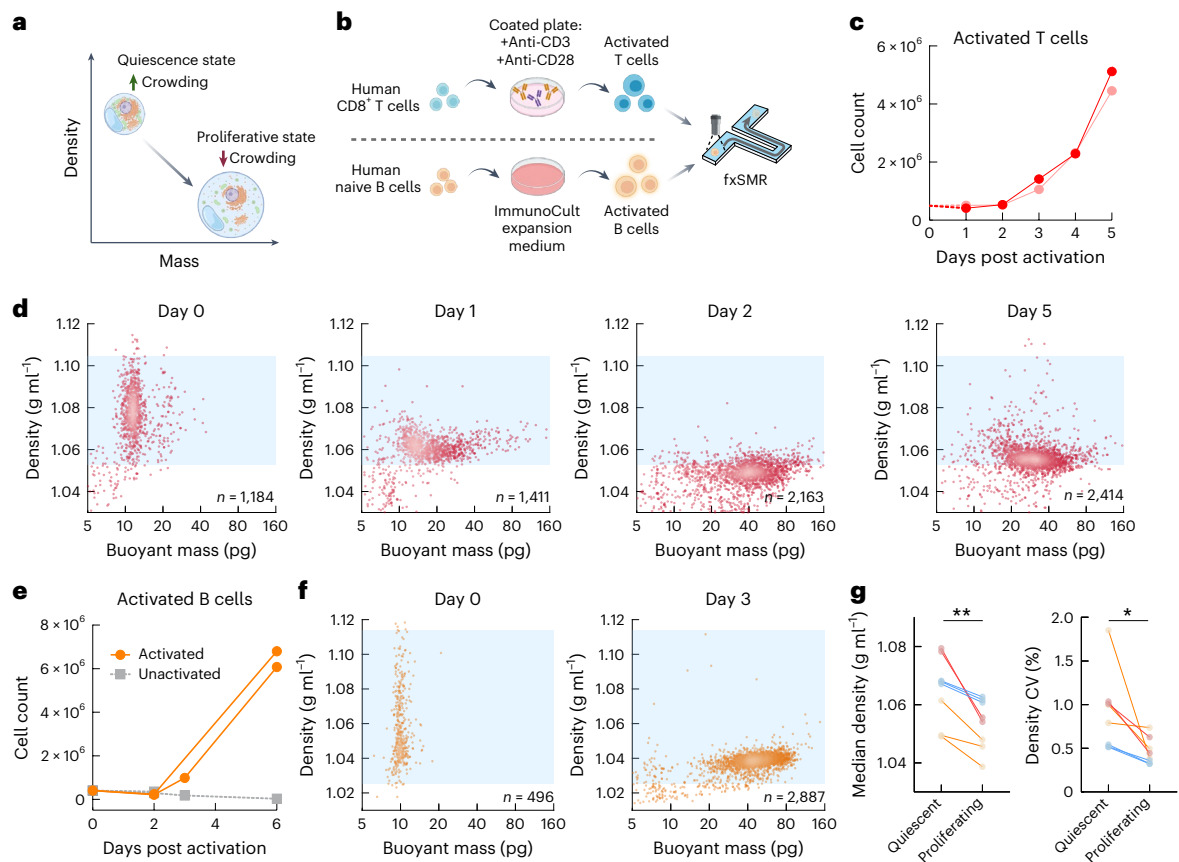


**Fig. 3 | Density profiling of human lymphocyte activation shows crowding transitions between quiescence and proliferative states.** **a**, A qualitative model of biophysical changes associated with the transition between quiescence and proliferative states. **b**, Schematics showing the activation process of human CD3<sup>+</sup>/CD8<sup>+</sup> T cell and human naive B cell and subsequent profiling by fxSMR. **c**, Cell count versus time (days post activation) for T cells obtained from two donors (red and pink). The dotted line denotes the expected seeding density. **d**, Scatter plots of mass versus density showing the T cell dynamics post activation for donor 1. The blue areas indicate the density range of quiescent T cells at day 0, with upper and lower bounds indicating the 1st and 99th percentile of the density distribution. CVs of density at day 0, 1, 2 and 5 are 1.008%, 0.453%, 0.392% and 0.627%, respectively. *n* refers to the number of individual cells.

**e**, Representative cell count versus time (days post activation) for naive B cells obtained from two donors. The B cells were either activated (solid orange lines) or kept as inactive naive B cells (dotted grey line). **f**, Representative scatter plots of mass versus density showing B cells at day 0 and 3 post activation. The blue areas indicate the density range of quiescent B cells similar to **d**. CVs of density at day 0 and 3 are 1.850% and 0.384%, respectively. *n* refers to the number of individual cells. **g**, The median cell density and the CV of density for quiescent and proliferating lymphocytes. Two-tailed paired *t*-tests yielded *P* values of 0.0049 for median density 0.0269 for density CV, from eight biological replicates, including T cells (red), B cells (orange) and murine pro-B lymphocytic cell line FL5.12 (blue). Figure created with [BioRender.com](https://www.biorender.com).

First, we studied human lymphocytes from peripheral blood that circulate as quiescent cells and can readily become activated and proliferating effector cells after encountering external stimuli. We performed daily measurements of CD8<sup>+</sup> T cells from two human donors after anti-CD3 and anti-CD28 activation (Fig. 3b,c). During the first 2 days post activation, the density CV decreased from ~1% to ~0.4%, suggesting a stronger density regulation as T cells start to proliferate (Chi-square variance tests reported *P* values < 0.00001 for both donors) (Supplementary Fig. 4g). In the same time frame, T cells increased their size substantially while decreasing average density from ~1.08 to ~1.05 g ml<sup>-1</sup> (Fig. 3d,g and Supplementary Fig. 4a). We then sought to determine whether this decrease in average cell density reflects changes in molecular crowding. As a proxy for molecular crowding, we measured the fraction of osmotically active water content over total cell volume by applying the Boyle Van't Hoff relation, where the volume of a cell is inversely proportional to the external osmolality<sup>36–38</sup>. We measured the active water content of T cells by profiling the volumes of each sample under two different osmolarity conditions (Supplementary Fig. 4b). We found that T cells increased their water content from ~63% to ~80% of total cell volume within the first 2 days of activation (Supplementary

Fig. 4c,d), suggesting a lower crowding level before cells start to divide. The relationship between cell density and intracellular molecular concentrations is discussed in more detail in Supplementary Note 3.

We confirmed our findings by studying different cellular models of cell quiescence and proliferation. Similar trends in cell density and size were observed in activated and proliferative human naive B cells (Fig. 3b,e–g and Supplementary Fig. 4e–g). In addition, we studied a pro-B lymphocytic murine cell line FL5.12, which is interleukin-3 (IL-3) dependent and exits the cell cycle following IL-3 depletion<sup>39</sup>. As with the human lymphocytes, we observed that quiescent FL5.12 cells have a higher density owing to increased crowding and higher density CV when compared with their proliferative state (Fig. 3g and Supplementary Fig. 5). We performed small particle trapping experiments to validate that the observed differences in density CV are predominantly driven by biological variability rather than increased measurement noise in small quiescent cells (Supplementary Note 1). Overall, our results reveal that lymphocytes maintain lower cell density and tighter density homeostasis when proliferating. This suggests that density regulation is coupled to the molecular machinery responsible for cell growth and/or proliferation.

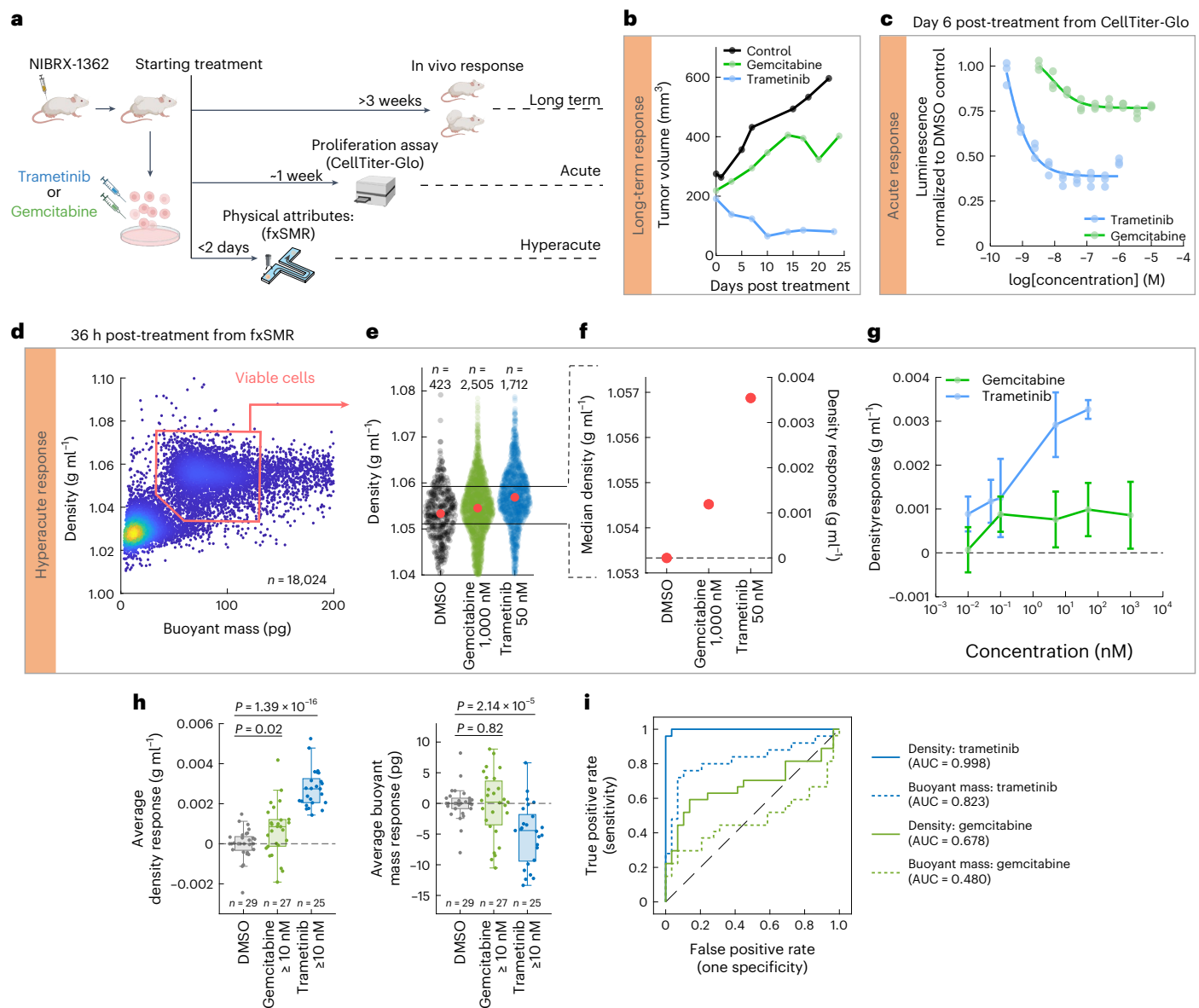


**Fig. 4 | Density demonstrates robustness as a hyperacute biomarker for predicting long-term in vivo drug response.** **a**, Schematics showing the paradigm of functional biomarkers for predicting long-term in vivo treatment response. **b**, The in vivo treatment response measured by tumour volume (one mouse per condition) data<sup>47</sup>. **c**, CellTiter-Glo dose response at day 6 after treatment, with three biological replicates per drug concentration. The slopes represent dose response fitting. **d**, Representative scatter plot of single-cell mass versus density at 36 h post treatment. The red box shows the gating of viable cells. *n* refers to the number of individual cells. **e**, Viable single-cell densities, with red dots denoting the median densities. **f**, Calculation of density response, with the dotted line indicating where the density response is 0 (median density equal to the DMSO control). **g**, The 36 h density responses for gemcitabine and trametinib

at multiple concentrations. Data indicate mean  $\pm$  s.e.m.; *n* = 3, 3, 4, 4 and 6 biological replicates for ascending concentrations of gemcitabine, and *n* = 3, 3, 3, 4 and 5 biological replicates for ascending concentrations of trametinib. **h**, The average density (left) and buoyant mass (right) responses following different treatments. The *P* values were generated from two-sided unpaired parametric *t*-tests. On each box and whiskers plot, the central mark denotes the median, the edges represent the 25th/75th percentiles and the whiskers extend to 1.5 $\times$  the interquartile range away from the box edges. *n* denotes the number of biological replicates. **i**, The ROC analysis of density (solid lines) and buoyant mass (dotted lines) responses using data from **h**. The area under the curve (AUC) scores denote the predictive powers of density and mass response. Figure created with BioRender.com.

### Density as a biomarker for drug response

Since changes in cell density can reveal state transitions related to cell proliferation, we sought to determine whether it could be used as a biomarker for assessing the ex vivo treatment response of cancer cells. A major goal for precision cancer medicine is to match each patient with the most effective drug treatment. Functional precision medicine (FPM) approaches, which involve drug testing performed directly on patient tumour cells, have emerged in recent years to help select the optimal drug treatment at the time of diagnosis or relapse<sup>40</sup>. In these assays, live cells isolated from patient tumours are treated with a panel

of candidate drugs ex vivo, and drug responses are assessed for their ability to predict patient outcomes<sup>41</sup>. Proliferation-based assays for drug response work well in cell line models that have adapted to thrive in ex vivo conditions. However, primary cancer cells often do not proliferate or require specific culture conditions to stimulate proliferation ex vivo, thereby increasing risk of phenotypic drift<sup>42</sup>. Consequently, there is a need for predictive FPM biomarkers that minimize phenotypic drift by assessing ex vivo treatment response at short timescales where cells are not proliferating. A number of studies have shown that cell mass can function as a predictive biomarker with 1–2 day turnaround times<sup>21,22,43,44</sup>.

We hypothesized that cell density response could also function as a hyperacute predictive biomarker even in the absence of proliferation, given that increases in crowding level (that is, cytoplasmic condensation) have long been regarded as an early indicator of apoptosis<sup>18,45,46</sup>.

To validate the density biomarker, we used a patient-derived xenograft (PDX) model as a source of cells to benchmark the density response against previously established FPM assays of proliferation and cell mass measurements (Fig. 4a). The pancreatic ductal adenocarcinoma model, NIBRX-1362, harbours the KRAS G12D mutation and has known *in vivo* drug response profiles from a previous study<sup>47</sup> (Fig. 4b). Repeat testing confirmed the model exhibited *in vivo* sensitivity to trametinib, a MEK pathway inhibitor, and only mild response to gemcitabine, a chemotherapy. We next isolated dissociated single cells derived from the untreated PDX tumours and assessed proliferation response using CellTiter-Glo at 6 days after *ex vivo* drug treatment. Using this approach, we noted a marked *ex vivo* tumour cell response to trametinib and a less effective response to gemcitabine (half-maximum inhibitory concentration of 0.172 nM and 8.561 nM, respectively) (Fig. 4c) thereby validating that the *ex vivo* response agreed with the *in vivo* results at an 'acute' 6 day time frame.

To determine whether single-cell density can achieve the same conclusion but at a hyperacute timescale, we profiled single-cell density and mass using fxSMR at 24 and/or 36 h post drug treatment, using similar conditions to the CellTiter-Glo assay. We first applied a gating based on density and buoyant mass to select viable cells (Fig. 4d and Supplementary Note 2), and then for every drug-treated sample, we subtracted the median density of the sample from the median density of the control (Fig. 4e,f) to obtain a density response for each treatment. A dose-response analysis demonstrated that both trametinib and gemcitabine resulted in density response when compared with the dimethylsulfoxide (DMSO) treatment ( $n = 9$  separate experiments and PDX-bearing mice). The half-maximum effective concentration for trametinib treatment was 0.017 nM, and could not be stably fitted for gemcitabine treatment (Fig. 4g). At high concentrations ( $\geq 10$  nM), trametinib treatments displayed a greater and more significant density response compared with gemcitabine (median density response of 0.0027 g ml<sup>-1</sup> and 0.0009 g ml<sup>-1</sup>, accordingly), which agreed with the long-term *in vivo* response and the CellTiter-Glo results (Fig. 4h).

Furthermore, when benchmarking the ability to distinguish between treatment responses, we found that buoyant mass detected a significant response from trametinib treatment, but could not resolve a significant gemcitabine response (Fig. 4h). To further test whether the density response is more likely to align with the long-term *in vivo* response, we performed a receiver operating characteristic (ROC) analysis on the robustness of a binary prediction of the PDX model's *in vivo* treatment sensitivity, generated from comparisons of *ex vivo* drug response against the DMSO control (Fig. 4i). The ROC analysis showed that, for both treatments, density has a stronger predictive power than mass (for trametinib, density AUC of 0.998 and mass AUC of 0.823; for gemcitabine, density AUC of 0.678 and mass AUC of 0.480). Since fxSMR readouts were collected from a cohort of nine replicates of the PDX model, the strong AUC score for predicting trametinib response also suggests that *ex vivo* cell density response is highly robust in resolving the long-term *in vivo* response of an effective treatment observed in this PDX model.

## Discussion

We have shown that fxSMR can precisely measure single-cell density with 10–100× higher throughput than existing methods. With our approach, we discovered that cell density and molecular crowding differ between proliferating and quiescent lymphocytes. This discovery bears resemblance to similar observations in unicellular organisms, where the increased molecular crowding in the quiescence state has been associated with slower signalling and lowered metabolic activity<sup>4,5,48</sup>. It is possible that the high cell density we observed in quiescent mammalian cells has a similar role where non-proliferating and largely inactive

cells conserve energy. More broadly, our results suggest a conserved mechanism that couples the regulation of cell density and molecular crowding to the regulation of cell state between quiescence and proliferation. It is also worth noting that a seemingly small change in cell density (<5%) can correspond to relatively large changes in molecular concentrations inside the cell, with potential implications for phase transitions and enzymatic reaction rates (Supplementary Note 3).

Our results also reveal insights into the regulation of cell density homeostasis. We discovered that proliferating mammalian cells display less cell-to-cell density variability than quiescent cells, indicating that the strength of density homeostasis is dependent on the cell cycle machinery responsible for cycling cell state. However, cells in early and late interphase display similar density homeostasis, ruling out density regulation by a G1, S or G2 cell cycle stage specific mechanism. Furthermore, our work revealed that cell density distributions are non-Gaussian in proliferating cells, thus narrowing down the space of theoretical models that could explain how density homeostasis is maintained.

In addition to its potential for exploration of the biology of density homeostasis, our approach may provide a much-needed method for functional precision medicine in patients. The ability of high-throughput single-cell density measurements to generate drug response data in the hyperacute non-proliferative window is a unique capability when compared with other functional precision medicine approaches. For example, organoid testing typically requires longer time periods (for example, weeks) for *ex vivo* expansion to generate a sufficient number of cells for assessments.

There are two important limitations of our drug response study. First, since we have not measured density response across multiple patient models, the broader predictive capability across heterogeneous cancers will require future studies. Second, since we have only measured the density response from two drugs, the extent to which density response will generalize across other drugs with a wide range of mechanisms remains unknown. However, previous studies with cell lines have shown that drugs with various mechanisms of action can uniformly perturb cell density<sup>18,19</sup>. With our high-throughput approach, we believe that many drugs can now be more readily profiled on patient samples within a hyperacute time window, thereby enabling clinical studies for assessing the effectiveness of density response in guiding patient treatment.

## Methods

### System set up

The design of the SMR devices were reported in ref. 49. The fabrication was carried out at CEA-LETI in Grenoble, France, with procedures outlined in refs. 17,26. An SMR device was actuated by a piezo-ceramic plated underneath the chip, which allows the suspended cantilever to vibrate at the resonant frequency of its second vibrational mode. Vibrational frequencies were measured by piezo resistors at the base of the cantilever. A closed-loop feedback system was applied to ensure consistent actuation at the resonant frequency, with a predefined delay time between the piezo resistor readout signal and the actuator driving signal. The driving signal was amplified to achieve high-oscillation amplitude as well as low-frequency noise.

The optical set up was built with an epi-fluorescence microscope (Nikon LV-UEPI2), using similar designs as previously described<sup>50</sup>. To reduce the noise in fluorescence measurements resulting from mechanical instabilities, two additional optical posts (Thorlabs) were installed to better support the optical pedestal (Thorlabs) between the microscope and the lower breadboard that holds the SMR device. Fluorescence excitation was provided by a laser-LED multiband illuminator (Lumencor SPECTRA Light engine). A 50×/0.55 objective lens (Nikon-CFI, LU Plan ELWD WD 10.1 mm) was used, and the emission collection area was defined by two orthogonally placed adjustable mechanical slits (Thorlabs VA100/M). The emission light was collected using a complementary metal-oxide semiconductor camera (FLIR, BFS-U3-13Y3M-C) and photomultiplier tubes (Hamamatsu, H10722-20).

A 10/90 beam splitter was positioned in front of the camera to direct 10% of all emission light to the camera. For each photomultiplier tube, the light path consisted of a dichroic mirror (Semrock), an emission filter (Semrock) and a convex lens (Thorlabs LA1027). The emission light was separately collected into five PMTs with the following emission filter ranges: 438/24, 515/30, 595/31, 678/70 and 809/81 nm. Volume measurements from fluorescein isothiocyanate (FITC)-dextran dye molecules were conducted with -500 mW excitation light (475/28 nm) and the emission light was captured within the 515/30 nm band. The exact optics configurations are shown in Supplementary Fig. 6a. For communications with the PMTs, reference voltages were set by analogue output modules (National Instruments NI-9263) and the output signals were collected by voltage modules (National Instruments NI-9215) were used.

### System operation

SMR devices have four fluidic inlets that are connected to the sample, buffer and waste reservoirs with 0.007 inch inner-diameter fluorinated ethylene propylene tubing (IDEX Health & Science). Pressurized house air was used to drive the fluidics. Flow directions were controlled by electronic pressure regulators and solenoid valves, through a custom software in LabView2020. The typical flow rate was around  $-10 \text{ nl s}^{-1}$ , as estimated by the time for an average particle to travel through the SMR cantilever.

For a typical single-cell density measurement, cells were resuspended to a final concentration of  $-1 \text{ million cells ml}^{-1}$  in the fluorescent buffer. The buffer was made by dissolving 2,000 kDa FITC-dextran (Sigma, FD2000S) in PBS or cell culture media to a final concentration of  $10 \text{ mg ml}^{-1}$ . Each sample was typically measured for 15–20 min. Before each experiment, using a camera, we first manually set the location of the light excitation spot at the centre of the microfluidic channel, adjacent to the entrance to the SMR cantilever. Then, we adjusted the microscope aperture diaphragm to ensure that the excitation spot is wider than the microfluidic channel. During the run, the sample reservoir was stored on ice to minimize endo/exocytosis. After each measurement, the SMR cantilever was flushed with 50% bleach in water and subsequently with PBS to minimize any accumulation of debris or air bubbles along the channel wall. To ensure consistent volume measurement across different samples, we adjusted the positioning of rectangular slits at the start of each experiment to define the emission collection area (Supplementary Fig. 6b,c). Given that the channel height was fixed, the slits configuration determined the total fluorescence excitation volume, which was used to calculate cell volume. Slits configuration was usually set to  $20 \mu\text{m}$  (width) by  $40 \mu\text{m}$  (length) for a typical sample. The width was further adjusted for samples with very small average cell sizes (naive T cells), and large average cell sizes (s-Hela). Data acquisition was enabled by custom measurement software in LabView2020 for both SMR and optical readouts. SMR data were acquired at a data rate of  $-20 \text{ kHz}$  and light-intensity readouts from PMTs were acquired at a rate of  $-50 \text{ kHz}$ . Subsequent fxSMR data analysis is described in Supplementary Note 4

### Calibration of volume and buoyant mass measurement

Calibration of the raw volume signal from fxSMR to the standard unit (femtolitre) was done with the L1210 cell line. Before each experiment, we first measured a cell line population in PBS suspension using a coulter counter (Beckman Coulter Multisizer 4,  $100 \mu\text{m}$  aperture) to obtain a cell volume distribution with the standard unit. Then, we measured the cells using fxSMR and acquired a distribution of their raw volume signals. From these two distributions, we first took the median of each measurement and calculated their ratio as an estimated calibration factor (volume in fl/volume in a.u.). Then we refined the calibration accuracy by looping through a range of potential calibration factors ( $\pm 3 \text{ a.u.}$  around the starting calibration factor derived by medians) to minimize the difference between the two distributions (the summed

difference in probability density between each percentile in the distribution). This optimization step led to a final calibration factor. SMR frequency peaks were calibrated (hertz to picogram) with  $8 \mu\text{m}$  polystyrene beads with a known density of  $1.05 \text{ g ml}^{-1}$  (Thermo Fisher, Duke Standards). Calibration calculations for both cell volume and buoyant mass were conducted using MATLAB.

### Accuracy and precision characterization

We characterized the accuracy of fxSMR volume measurement by benchmarking against coulter counter volume measurement using five different cell lines, with median cell size ranges from  $-1,000$  to  $-5,000 \text{ fl}$ . The volume of each cell line sample was first determined by a Coulter Counter (Beckman) and subsequently measured by fxSMR. From the single-cell volume distributions measured by the two platforms, the median value of each sample was computed and used to calculate correlation score between fxSMR measurements and ground-truth cell volumes (Supplementary Fig. 1a,b). We characterized the accuracy of fxSMR buoyant mass measurement with NIST traceable polystyrene beads (Thermo Fisher) of five different sizes between  $5 \mu\text{m}$  and  $9 \mu\text{m}$  in diameter (Supplementary Fig. 1c,d). The precision of fxSMR was determined by repeatedly measuring the same hydrogel particle (deformable poly-acrylamide-co-acrylic acid microparticle), donated by the Morgan Huse lab at the Sloan Kettering Institute. Each particle was pushed forwards and backwards through the cantilever at the rate of  $-30 \text{ s}$  per measurement for a duration of  $-20 \text{ min}$ . The trapping mechanism was achieved by oscillating the pressure setting between the left and right side of the cantilever to generate forwards and backwards pressure gradients. Real-time SMR frequency analysis was used to recognize the passage of a particle and the pressure setting was then switched after a predefined period of time ( $50$ – $200 \text{ ms}$ ) after each passage. Fluidic controls were carried out through a custom software in LabView2020. The ground-truth particle size was determined from  $60\times$  brightfield images taken using an imaging flow cytometer (Amnis ImageStream, Cytek), with INSPIRE ImageStream System Software. Particle areas were calculated using automated feature identification using the IDEAS image analysis software. Particle volumes were subsequently calculated using GraphPad Prism. The simulation on the effects of measurement uncertainty on cell population density variability was written in MATLAB R2021a. The algorithm first defined input parameters, including the proposed mean cell density ( $\mu = 1.08$ ), sample size ( $n = 5,000$ ), the range of population CVs ( $0.1\%$  to  $1.2\%$ ) and the CVs of the measurement noise ( $0.033\%$  to  $0.294\%$ ). The algorithm then proceeded with two nested loops. The outer loop iterated through the predefined noise CV values, while the inner loop varied the population CV values. For each combination, the algorithm generated a cell density population using a normal distribution with the specified mean and standard deviation based on the current population CV. It then added Gaussian noise to each sample, with the noise standard deviation calculated as a product of the noise CV and the sample value. The mean and standard deviation of the simulated cell population were used to calculate the CV of the simulated density distribution. This computed CV was used to compare different combinations of population and measurement noise variability.

### Statistics

Statistical analysis was conducted using MATLAB and GraphPad Prism. Statistical significance between groups or different experimental conditions was determined using an unpaired parametric *t*-test in Fig. 4 and a paired parametric *t*-test in Fig. 3 and Supplementary Fig. 5. A Chi-square variance test for Supplementary Fig. 4g was performed with `vartest()` MATLAB function. Distribution fitting over single-cell data in Fig. 2 was conducted with the `fitdist()` MATLAB function with specification on distribution type such as normal, log-normal or stable. The kurtosis and skewness factor of single-cell distributions were calculated by `kurtosis()` and `skewness()` MATLAB functions. One-sample Kolmogorov–Smirnov tests in Supplementary Fig. 2a–c were conducted

by first fitting the data with the intended distribution type using the `fitdist()`, and then the `kstest()` MATLAB function was performed to test the data against the cumulative distribution function of the fitted model. Bootstrap analysis for Fig. 2 and Supplementary Fig. 2a–c was carried out with the `bootstrp()` MATLAB function with 1,000 iterations. ROC analysis in Fig. 4 was conducted with the `percurve()` MATLAB function. A binary sensitivity label was given as the outcome variable, with trametinib-treated samples as sensitive and gemcitabine-treated conditions as non-sensitive.

### Water content measurement by osmotic shocks

Osmotically active water content was measured by volume exclusion on *fxSMR*. We measured aliquots from the same sample population that were resuspended in different osmolarities. Isotonic buffer is the cell culture media containing 5 mg ml<sup>-1</sup> FITC–dextran, which has an estimated osmolarity of 300 mOsm. The 600 mOsm hyperosmolarity buffer was made by first diluting NaCl stock solution (Sigma S5150) with water to a final concentration of 225 mM NaCl in water, and then mixing the NaCl buffer with PBS that contains 10 mg ml<sup>-1</sup> FITC–dextran, with a 1:1 mixing ratio. After *fxSMR* volume measurements on the two buffer conditions, the median cell volume was calculated from each single-cell dataset. A linear regression fitting was conducted using median cell volumes as *y* values and the corresponding [1/osmolarity] as *x* values. The *y* intercept of the fitted slope was determined as the osmotically inactive volume, and osmotically active water content was determined by subtracting the inactive volume from the median cell volume of the isotonic measurement (Supplementary Fig. 4b).

### Cell culture

L1210, THP-1, BaF-3, FL5.12, s-HeLa and HL60 cells were cultured in RPMI (Invitrogen). Patu-8902 cells were cultured in Dulbecco's modified Eagle medium (DMEM) (Gibco). For all cells, the media was supplemented with 10% FBS (Sigma-Aldrich), 1 mM Na pyruvate (Invitrogen), 10 mM HEPES (Invitrogen) and antibiotics (Invitrogen). The FL5.12 cell culture media was also supplemented with 100 ng ml<sup>-1</sup> IL-3 (R&D Systems). L1210 cells were obtained from American Type Culture Collection, THP-1 cells were graciously donated by the Chen lab at MIT, BaF-3 cells were obtained from RIKEN BioResource Center, FL5.12 cells were previously donated by the Vander Heiden lab at MIT. s-HeLa cells were previously donated by the Elias lab at Brigham and Women's Hospital. HL60 cells were previously donated by Thiam lab at Stanford. Patu-8902 cells were previously donated by the Hahn lab at the Broad Institute. All experiments with cell lines were carried out with exponentially growing cells at a confluency of 300,000–600,000 cells ml<sup>-1</sup>. All cell lines were tested for mycoplasma and no mycoplasma was detected. For FL5.12 IL-3 depletion, cells were first grown to confluency at 1 million cells ml<sup>-1</sup>, and subsequently washed three times in RPMI media without IL-3 and resuspended in RPMI media without IL-3 at a concentration of 500,000 cells ml<sup>-1</sup>.

For CD8 T cell activation, apheresis leukoreduction collars from anonymous healthy platelet donors were obtained from the Brigham and Women's Hospital Specimen Bank under an institutional review board-exempt protocol. Human peripheral blood mononuclear cells (PBMCs) were isolated via density gradient centrifugation (Lymphoprep, StemCell Technologies Inc., 07801). PBMCs were resuspended in cryopreservation media (90% FBS + 10% DMSO) and frozen down. For T cell activation, 24-well plates were precoated with anti-human CD3 antibodies (0.5 µg ml<sup>-1</sup>, BioXCell, BE0001-2) and anti-human CD28 antibodies (5 µg ml<sup>-1</sup>, BioXCell, BE0248) for 24 h at 4 °C. PBMC samples were thawed on the day of activation and T cells were purified via the EasySep Human CD8<sup>+</sup> T Cell Enrichment kit (StemCell Technologies Inc., 19053). Isolated T cells were seeded in the CD3/CD28 precoated well plates at a concentration of 500,000 cells ml<sup>-1</sup> with 1 ml well<sup>-1</sup> in ImmunoCult-XF T Cell Expansion Medium (StemCell Technologies Inc., 10981) supplemented with 10 ng ml<sup>-1</sup>

recombinant IL-2 (StemCell Technologies Inc., 78036.1). T cells were removed from CD3/CD28 plate coating after 48 h of incubation and moved to uncoated wells. For the remainder of the culture, cells were passaged when the concentration reached over 1 million cells ml<sup>-1</sup> to a new concentration of 500,000 cells ml<sup>-1</sup>.

For B cell activation, apheresis leukoreduction collars from three anonymous healthy platelet donors were obtained from the Brigham and Women's Hospital Specimen Bank under an institutional review board-exempt protocol. PBMCs were isolated with Ficoll-Paque Plus (Thermo Fisher Scientific, 45001749) using the manufacturer's recommended protocol. The PBMC layer was isolated, subjected to ACK lysis (Life Technologies, A1049201) and washed with PBS. Naive B cells were isolated using EasySep Human Naive B Cell Isolation kit (StemCell, 17254) according to the manufacturer's protocol. The naive B cells were seeded at 100,000–250,000 cells ml<sup>-1</sup> in a 6-well plate and cultivated in the ImmunoCult Human B Cell Expansion kit (StemCell, 100-0645). The plating density was adjusted to 100,000 cells ml<sup>-1</sup> every 2–4 days and the viability was assessed by Trypan blue. Unstimulated naive B cells were cultivated in RPMI supplemented with 10% FBS and antibiotics. The immunophenotype was confirmed by flow cytometry. The cells were stained in Brilliant Stain Buffer (BD Biosciences, 566349) with the following dyes and antibodies diluted at their predetermined concentrations: Zombie Aqua (BioLegend, 423102; 1:500 dilution), anti-human CD19 (BD Biosciences, 564456; prediluted by supplier), anti-human IgD (BD Biosciences, 561314; prediluted by supplier), anti-human CD27 (BD Biosciences, 562513; prediluted by supplier), anti-human CD86 (BD Biosciences, 555665; prediluted by supplier), anti-human HLA-DR (BD Biosciences, 560743; prediluted by supplier), anti-human CD24 (BD Biosciences, 563401; prediluted by supplier) and anti-human CD38 (BD Biosciences, 555462; prediluted by supplier). The cells were then washed with PBS supplemented with 2% FBS and 0.2% EDTA. Stained cells were analysed on a BD LSR Fortessa flow cytometer (Dana-Farber Cancer Institute (DFCI) Flow Cytometry core) and data were collected using FACSDiva and analysed using FlowJo v10 software.

### PDX model development and ex vivo drug testing

The NIBRX-1362 pancreatic ductal adenocarcinoma PDX model was previously established and characterized<sup>47</sup> and was obtained from the DFCI Center for Patient Derived Models, which is a distributor of the model<sup>51</sup>. Mice are housed in the state-of-the-art animal care facility at the DFCI with housing environment regulated for a 12 h simulated light/dark cycle, temperatures of 65–75 °F (-18–23 °C) with 40–60% humidity. Briefly, the cryopreserved PDX seeds were thawed and rinsed with DMEM before being implanted in athymic nude mice (Taconic, NCRNU-F) in the presence of matrigel (Corning). When the tumour reached a palpable size, tumour volume was measured and monitored using a digital caliper. Tumours were collected when approaching 2,000 mm<sup>3</sup> and were serially passaged from collected tumour seeds. The identity of the NIBRX-1362 PDX model used in this study was confirmed via STR fingerprinting and key gene mutations (KRAS G12D) were verified via exome sequencing. The animal protocol was approved by the DFCI Institutional Care and Use Committee.

To perform the acute drug sensitivity assays, freshly collected PDX tumours were aseptically explanted from the flank and processed to remove necrotic tumour regions and mechanically dissociated into single cells using the Miltenyi Tumor Dissociation kit (Miltenyi, 130-095-929) and the GentleMax dissociator according to the manufacturer's instructions. The dissociated cells were filtered using a 0.2 µm strainer and subjected to mouse cell removal using a mouse cell depletion kit (Miltenyi, 130-104-694). The mouse-depleted tumour cells of NIBRX-1362 were plated at 1,250 cells per well with 40 µl of DMEM + 2% FBS (Gibco, 11965092 and Sigma, F2442) in 384-well opaque plates (Corning, 3570) for acute drug sensitivity measurement via the CellTiter-Glo (CTG) assay and plated at 75k cells per well with 3 ml of DMEM + 2% FBS in 6-well ultralow attachment plates (Corning, 3471) for *fxSMR* assays.

For acute drug sensitivity measurement using the CTG assay, the freshly plated PDX cells were incubated overnight before treatment with a concentration range of gemcitabine (10  $\mu$ M to 3.25 nM, SelleckChem S1714) or trametinib (1  $\mu$ M to 0.325 nM, SelleckChem S2673) using an automated drug dispenser (Tecan D300e Digital Dispenser). After 6 days of drug treatment, cells were examined using CellTiter-Glo 2.0 cell viability assay (Promega G9241) according to the manufacturer's instruction. Data were analysed using GraphPad Prism.

### Reporting summary

Further information on research design is available in the Nature Portfolio Reporting Summary linked to this article.

### Data availability

All datasets generated in this study (single-cell buoyant mass, volume and density data, lymphocyte cell count data, as well as other measured variables) are available via Zenodo at <https://doi.org/10.5281/zenodo.15098741> (ref. 52). Source data are provided with this paper.

### Code availability

All codes used in this study are available via GitHub at [https://github.com/rwu0614/fluorescence\\_exclusion\\_fxSMR](https://github.com/rwu0614/fluorescence_exclusion_fxSMR) (ref. 53).

### References

- Neurohr, G. E. & Amon, A. Relevance and regulation of cell density. *Trends Cell Biol.* **30**, 213–225 (2020).
- Dill, K. A., Ghosh, K. & Schmit, J. D. Physical limits of cells and proteomes. *Proc. Natl Acad. Sci. USA* **108**, 17876–17882 (2011).
- Mourão, M. A., Hakim, J. B. & Schnell, S. Connecting the dots: the effects of macromolecular crowding on cell physiology. *Biophys. J.* **107**, 2761–2766 (2014).
- Miermont, A. et al. Severe osmotic compression triggers a slowdown of intracellular signaling, which can be explained by molecular crowding. *Proc. Natl Acad. Sci. USA* **110**, 5725–5730 (2013).
- Parry, B. R. et al. The bacterial cytoplasm has glass-like properties and is fluidized by metabolic activity. *Cell* **156**, 183–194 (2014).
- Shi, H. et al. Starvation induces shrinkage of the bacterial cytoplasm. *Proc. Natl Acad. Sci. USA* **118**, e2104686118 (2021).
- Munder, M. C. et al. A pH-driven transition of the cytoplasm from a fluid- to a solid-like state promotes entry into dormancy. *eLife* **5**, e09347 (2016).
- Sakai, K., Kondo, Y., Goto, Y. & Aoki, K. Cytoplasmic fluidization contributes to breaking spore dormancy in fission yeast. *Proc. Natl Acad. Sci. USA* **121**, e2405553121 (2024).
- Durmus, N. G. et al. Magnetic levitation of single cells. *Proc. Natl Acad. Sci. USA* **112**, E3661–E3668 (2015).
- Ge, S., Wang, Y., Deshler, N. J., Preston, D. J. & Whitesides, G. M. High-throughput density measurement using magnetic levitation. *J. Am. Chem. Soc.* **140**, 7510–7518 (2018).
- Figueroa, B., Xu, F. X., Hu, R., Men, S. & Fu, D. Quantitative imaging of intracellular density with ratiometric stimulated raman scattering microscopy. *J. Phys. Chem. B* **126**, 7595–7603 (2022).
- Oldewurtel, E. R., Kitahara, Y. & van Teeffelen, S. Robust surface-to-mass coupling and turgor-dependent cell width determine bacterial dry-mass density. *Proc. Natl. Acad. Sci. USA* **118**, e2021416118 (2021).
- Odermatt, P. D. et al. Variations of intracellular density during the cell cycle arise from tip-growth regulation in fission yeast. *eLife* **10**, e64901 (2021).
- Zlotek-Zlotkiewicz, E., Monnier, S., Cappello, G., Le Berre, M. & Piel, M. Optical volume and mass measurements show that mammalian cells swell during mitosis. *J. Cell Biol.* **211**, 765–774 (2015).
- Oh, S. et al. Protein and lipid mass concentration measurement in tissues by stimulated Raman scattering microscopy. *Proc. Natl Acad. Sci. USA* **119**, e2117938119 (2022).
- Liu, X., Oh, S. & Kirschner, M. W. The uniformity and stability of cellular mass density in mammalian cell culture. *Front. Cell Dev. Biol.* **10**, 1017499 (2022).
- Burg, T. P. et al. Weighing of biomolecules, single cells and single nanoparticles in fluid. *Nature* **446**, 1066–1069 (2007).
- Grover, W. H. et al. Measuring single-cell density. *Proc. Natl Acad. Sci. USA* **108**, 10992–10996 (2011).
- Byun, S., Hecht, V. C. & Manalis, S. R. Characterizing cellular biophysical responses to stress by relating density, deformability, and Size. *Biophys. J.* **109**, 1565–1573 (2015).
- Son, S. et al. Resonant microchannel volume and mass measurements show that suspended cells swell during mitosis. *J. Cell Biol.* **211**, 757–763 (2015).
- Kimmerling, R. J. et al. A pipeline for malignancy and therapy agnostic assessment of cancer drug response using cell mass measurements. *Commun. Biol.* **5**, 1295 (2022).
- Polanco, E. R. et al. Multiparametric quantitative phase imaging for real-time, single cell, drug screening in breast cancer. *Commun. Biol.* **5**, 794 (2022).
- Murray, G. F. et al. QPI allows in vitro drug screening of triple negative breast cancer PDX tumors and fine needle biopsies. *Front. Phys.* **7**, 158 (2019).
- Gray, M. L., Hoffman, R. A. & Hansen, W. P. A new method for cell volume measurement based on volume exclusion of a fluorescent dye. *Cytometry* **3**, 428–434 (1983).
- Cadart, C. et al. Fluorescence eXclusion measurement of volume in live cells. *Methods Cell. Biol.* **139**, 103–120 (2017).
- Lee, J. et al. Suspended microchannel resonators with piezoresistive sensors. *Lab Chip* **11**, 645–651 (2011).
- Fossion, R., Sáenz Burrola, A. & Zapata Fonseca, L. On the stability and adaptability of human physiology: Gaussians meet heavy-tailed distributions. *Interdiscip.* **8**, 55–81 (2020).
- Mu, L. et al. Mass measurements during lymphocytic leukemia cell polyploidization decouple cell cycle- and cell size-dependent growth. *Proc. Natl Acad. Sci. USA* **117**, 15659–15665 (2020).
- Limpert, E., Stahel, W. A. & Abbt, M. Log-normal distributions across the sciences: keys and clues. *Bioscience* **51**, 341 (2001).
- Ginzberg, M. B. et al. Cell size sensing in animal cells coordinates anabolic growth rates and cell cycle progression to maintain cell size uniformity. *eLife* **7**, e26957 (2018).
- Soifer, I., Robert, L. & Amir, A. Single-cell analysis of growth in budding yeast and bacteria reveals a common size regulation strategy. *Curr. Biol.* **26**, 356–361 (2016).
- Kafri, R. et al. Dynamics extracted from fixed cells reveal feedback linking cell growth to cell cycle. *Nature* **494**, 480–483 (2013).
- Cadart, C. et al. Size control in mammalian cells involves modulation of both growth rate and cell cycle duration. *Nat. Commun.* **9**, 3275 (2018).
- Miettinen, T. P., Ly, K. S., Lam, A. & Manalis, S. R. Single-cell monitoring of dry mass and dry mass density reveals exocytosis of cellular dry contents in mitosis. *eLife* **11**, e76664 (2022).
- Neurohr, G. E. et al. Excessive cell growth causes cytoplasm dilution and contributes to senescence. *Cell* **176**, 1083–1097.e18 (2019).
- Roffay, C. et al. Passive coupling of membrane tension and cell volume during active response of cells to osmosis. *Proc. Natl Acad. Sci. USA* **118**, e2103228118 (2021).
- Finan, J. D., Chalut, K. J., Wax, A. & Guilak, F. Nonlinear osmotic properties of the cell nucleus. *Ann. Biomed. Eng.* **37**, 477–491 (2009).
- Nobel, P. S. The Boyle-van't Hoff relation. *J. Theor. Biol.* **23**, 375–379 (1969).
- Hecht, V. C. et al. Biophysical changes reduce energetic demand in growth factor-deprived lymphocytes. *J. Exp. Med.* **213**, 2133OIA13 (2016).

40. Kornauth, C. et al. Functional precision medicine provides clinical benefit in advanced aggressive hematologic cancers and identifies exceptional responders. *Cancer Discov.* **12**, 372–387 (2022).
41. Letai, A. Functional precision cancer medicine—moving beyond pure genomics. *Nat. Med.* **23**, 1028–1035 (2017).
42. Raghavan, S. et al. Microenvironment drives cell state, plasticity, and drug response in pancreatic cancer. *Cell* **184**, 6119–6137.e26 (2021).
43. Stockslager, M. A. et al. Functional drug susceptibility testing using single-cell mass predicts treatment outcome in patient-derived cancer neurosphere models. *Cell Rep.* **37**, 109788 (2021).
44. Liu, X. et al. Characterizing dry mass and volume changes in human multiple myeloma cells upon treatment with proteotoxic and genotoxic drugs. *Clin. Exp. Med.* **23**, 3821–3832 (2023).
45. Ernest, N. J., Habela, C. W. & Sontheimer, H. Cytoplasmic condensation is both necessary and sufficient to induce apoptotic cell death. *J. Cell Sci.* **121**, 290–297 (2008).
46. Van Cruchten, S. & Van Den Broeck, W. Morphological and biochemical aspects of apoptosis, oncosis and necrosis. *Anat. Histol. Embryol.* **31**, 214–223 (2002).
47. Gao, H. et al. High-throughput screening using patient-derived tumor xenografts to predict clinical trial drug response. *Nat. Med.* **21**, 1318–1325 (2015).
48. Petrovska, I. et al. Filament formation by metabolic enzymes is a specific adaptation to an advanced state of cellular starvation. *eLife* **3**, e02409 (2014).
49. Kang, J. H. et al. Noninvasive monitoring of single-cell mechanics by acoustic scattering. *Nat. Methods* **16**, 263–269 (2019).
50. Kang, J. H. et al. Monitoring and modeling of lymphocytic leukemia cell bioenergetics reveals decreased ATP synthesis during cell division. *Nat. Commun.* **11**, 4983 (2020).
51. Dana-Farber Cancer Institute. Ordering and Licensing CPDM's Patient Derived Models (PDX, PDCL). <https://www.dana-farber.org/research/departments-centers-and-labs/integrative-research-centers/center-for-patient-derived-models/ordering-patient-derived-models/> (2025).
52. Wu, W. Source data for article 'High-throughput single-cell density measurements enable dynamic profiling of immune cell and drug response from patient samples'. *Zenodo* <https://doi.org/10.5281/ZENODO.15098741> (2025).
53. Wu, W. Fluorescence\_exclusion\_fxSMR: analysis of raw FxSMR data. *GitHub* [https://github.com/rwu0614/fluorescence\\_exclusion\\_fxSMR](https://github.com/rwu0614/fluorescence_exclusion_fxSMR) (2021).
- for Cancer Research, MIT Center for Precision Cancer Medicine, Stand Up to Cancer (SU2C) Convergence Program 3.1416, and R01 GM150901 from the US National Institutes of Health. K.L.L. and S.R.M. disclose support for the research described in this study from Bristol Myers Squibb. This work was also supported in part by the Koch Institute Support (core) Grant P30-CA014051 from the National Cancer Institute.

### Author contributions

W.W., T.P.M., K.L.L. and S.R.M. conceptualized the study. W.W. and S.H.I. designed and built the measurement device with assistance from T.P.M. and Y.Z. For accuracy and precision characterizations, T.P.M. carried out cell culture work, and W.W. and S.H.I. performed fxSMR measurement and data analysis. For the lymphocyte study, S.M.D. and L.L.D. carried out the cell culture work, and W.W. and Y.Z. carried out fxSMR measurement and data analysis. For the PDX study, T.W.Q., S.Y., P.-L.K. and K.-H.C. carried out all in vivo, CTG and cell culture work, and W.W. and S.H.I. performed fxSMR measurement and data analysis. W.W. wrote the paper with contributions from M.A.M., M.M., T.P.M., K.L.L. and S.R.M. All authors reviewed and approved the paper.

### Competing interests

S.R.M. and K.L.L. are founders of Travera. S.R.M. is a founder of Affinity Biosensors. K.L.L. receives consulting fees from Bristol Myers Squibb, Blaze Bioscience, and Integragen. MIT has filed a patent application (PCT/US2022/051503) on the method for measuring single-cell density, with S.R.M., W.W. and T.P.M. listed as the inventors. MIT and DFCI have joint filed a patent application (PCT/US2022/051514) on single-cell density as a biomarker for drug response, with S.R.M., K.L.L., W.W., T.P.M., S.H.I. and K.-H.C. listed as the inventors. The other authors declare no competing interests

### Additional information

**Supplementary information** The online version contains supplementary material available at <https://doi.org/10.1038/s41551-025-01408-6>.

**Correspondence and requests for materials** should be addressed to Keith L. Ligon or Scott R. Manalis.

**Peer review information** *Nature Biomedical Engineering* thanks Dayong Jin, Thomas Zangle and the other, anonymous, reviewer(s) for their contribution to the peer review of this work.

**Reprints and permissions information** is available at [www.nature.com/reprints](http://www.nature.com/reprints).

**Publisher's note** Springer Nature remains neutral with regard to jurisdictional claims in published maps and institutional affiliations.

Springer Nature or its licensor (e.g. a society or other partner) holds exclusive rights to this article under a publishing agreement with the author(s) or other rightsholder(s); author self-archiving of the accepted manuscript version of this article is solely governed by the terms of such publishing agreement and applicable law.

© The Author(s), under exclusive licence to Springer Nature Limited 2025

### Acknowledgements

We thank M. Huse (Sloan Kettering Institute) for donating DAAM-particles, J. Chen (Koch Institute) for donating THP-1 cells, M. Vander Heiden (Koch Institute) for donating FL5.12 cells, K. Elias (Brigham and Women's Hospital) for donating s-HeLa cells, H. Thiam (Stanford) for donating HL60 cells and B. Hahn (Broad Institute) for donating Patu-8902 cells. We thank the Koch Institute's Robert A. Swanson (1969) Biotechnology Center for technical support, specifically The Swanson Biotechnology Center Flow Cytometry Facility. S.R.M. discloses support for the research described in this study from Paul G. Allen Frontiers Group, Virginia and D.K. Ludwig Fund

<sup>1</sup>Koch Institute for Integrative Cancer Research, Massachusetts Institute of Technology, Cambridge, MA, USA. <sup>2</sup>Department of Biological Engineering, Massachusetts Institute of Technology, Cambridge, MA, USA. <sup>3</sup>Center for Patient-Derived Models, Dana-Farber Cancer Institute, Boston, MA, USA.

<sup>4</sup>Department of Pathology, Dana-Farber Cancer Institute, Harvard Medical School, Boston, MA, USA. <sup>5</sup>Department of Medical Oncology, Dana-Farber Cancer Institute, Boston, MA, USA. <sup>6</sup>Bristol Myers Squibb, Cambridge, MA, USA. <sup>7</sup>Broad Institute of Harvard and MIT, Cambridge, MA, USA. <sup>8</sup>Department of Pathology, Brigham and Women's Hospital, Harvard Medical School, Boston, MA, USA. <sup>9</sup>Department of Pathology, Boston Children's Hospital, Harvard Medical School, Boston, MA, USA. <sup>10</sup>Department of Mechanical Engineering, Massachusetts Institute of Technology, Cambridge, MA, USA.

✉ e-mail: [keith\\_ligon@dfci.harvard.edu](mailto:keith_ligon@dfci.harvard.edu); [srm@mit.edu](mailto:srm@mit.edu)

## Reporting Summary

Nature Portfolio wishes to improve the reproducibility of the work that we publish. This form provides structure for consistency and transparency in reporting. For further information on Nature Portfolio policies, see our [Editorial Policies](#) and the [Editorial Policy Checklist](#).

### Statistics

For all statistical analyses, confirm that the following items are present in the figure legend, table legend, main text, or Methods section.

n/a Confirmed

- The exact sample size ( $n$ ) for each experimental group/condition, given as a discrete number and unit of measurement
- A statement on whether measurements were taken from distinct samples or whether the same sample was measured repeatedly
- The statistical test(s) used AND whether they are one- or two-sided  
*Only common tests should be described solely by name; describe more complex techniques in the Methods section.*
- A description of all covariates tested
- A description of any assumptions or corrections, such as tests of normality and adjustment for multiple comparisons
- A full description of the statistical parameters including central tendency (e.g. means) or other basic estimates (e.g. regression coefficient) AND variation (e.g. standard deviation) or associated estimates of uncertainty (e.g. confidence intervals)
- For null hypothesis testing, the test statistic (e.g.  $F$ ,  $t$ ,  $r$ ) with confidence intervals, effect sizes, degrees of freedom and  $P$  value noted  
*Give  $P$  values as exact values whenever suitable.*
- For Bayesian analysis, information on the choice of priors and Markov chain Monte Carlo settings
- For hierarchical and complex designs, identification of the appropriate level for tests and full reporting of outcomes
- Estimates of effect sizes (e.g. Cohen's  $d$ , Pearson's  $r$ ), indicating how they were calculated

*Our web collection on [statistics for biologists](#) contains articles on many of the points above.*

### Software and code

Policy information about [availability of computer code](#)

- Data collection 

SMR and PMT data were collected using National Instrument LabVIEW 2020 SP1 (32bit). Flow cytometer data was collected using BD FACSDiva software (v7). Cell volume and cell count data were collected using Beckman Coulter Multisizer 4 software (v4.01). Single hydrogel particle images were collected using INSPIRE ImageStream System Software (version not published by supplier) and analyzed using IDEAS software (v6).
- Data analysis 

MATLAB R2021a was used for SMR and PMT data analysis, plotting, statistical tests, and simulation. FlowJo v10 was used for flow cytometer data analysis. GraphPad Prism v9.5.0 was used for plotting data and statistical tests.

For manuscripts utilizing custom algorithms or software that are central to the research but not yet described in published literature, software must be made available to editors and reviewers. We strongly encourage code deposition in a community repository (e.g. GitHub). See the Nature Portfolio [guidelines for submitting code & software](#) for further information.

## Data

Policy information about [availability of data](#)

All manuscripts must include a [data availability statement](#). This statement should provide the following information, where applicable:

- Accession codes, unique identifiers, or web links for publicly available datasets
- A description of any restrictions on data availability
- For clinical datasets or third party data, please ensure that the statement adheres to our [policy](#)

All data generated in this study ( single-cell buoyant mass, volume and density data, lymphocyte cell count data, as well as other measured variables) are published and available at <https://doi.org/10.5281/zenodo.15098741>

## Research involving human participants, their data, or biological material

Policy information about studies with [human participants or human data](#). See also policy information about [sex, gender \(identity/presentation\), and sexual orientation](#) and [race, ethnicity and racism](#).

Reporting on sex and gender	Sex and gender information was not collected as the lymphocyte samples were from anonymous healthy platelet donors.
Reporting on race, ethnicity, or other socially relevant groupings	Information on race, ethnicity, or other socially relevant groupings was not collected as the lymphocyte samples were from anonymous healthy platelet donors.
Population characteristics	See above
Recruitment	Apheresis leukoreduction collars from anonymous healthy platelet donors were obtained from the Brigham and Women's Hospital Specimen Bank
Ethics oversight	Sample collection was performed under an Institutional Review Board–exempt protocol

Note that full information on the approval of the study protocol must also be provided in the manuscript.

## Field-specific reporting

Please select the one below that is the best fit for your research. If you are not sure, read the appropriate sections before making your selection.

- Life sciences       Behavioural & social sciences       Ecological, evolutionary & environmental sciences

For a reference copy of the document with all sections, see [nature.com/documents/nr-reporting-summary-flat.pdf](https://www.nature.com/documents/nr-reporting-summary-flat.pdf)

## Life sciences study design

All studies must disclose on these points even when the disclosure is negative.

Sample size	No statistical tests were used to determine the sample size. All experiments with hydrogel beads, cell lines and PDX samples relied on three or more independent samples, which was considered sufficient to determine any major effects. For lymphocyte activation experiment, two T cell donors and three B cell donors were selected as they all represent primary human lymphocytes. These sample sizes were selected based on standard practices in the field and practical considerations including sample availability and experimental feasibility.
Data exclusions	Some fxSMR data was excluded with a pre-established exclusion criteria to ensure confidence in signal quality. For full details of data exclusion, please see Supplementary Note 4.
Replication	All cell line and PDX data displayed represents at least three independent samples. For determining fxSMR precision, each particles were repeatedly measured at least 40 times.
Randomization	For single-cell fxSMR experiments, the cells that were measured were randomly selected by loading a population of cells into the fxSMR device. For isolated primary cells from human donors and PDX models, cells were randomly selected to receive activation or drug treatments.
Blinding	No blinding was carried out, since experiments and data analysis were carried out by the same group of individuals.

## Reporting for specific materials, systems and methods

We require information from authors about some types of materials, experimental systems and methods used in many studies. Here, indicate whether each material, system or method listed is relevant to your study. If you are not sure if a list item applies to your research, read the appropriate section before selecting a response.

## Materials &amp; experimental systems

n/a	<input type="checkbox"/>	Involvement in the study
<input type="checkbox"/>	<input checked="" type="checkbox"/>	Antibodies
<input type="checkbox"/>	<input checked="" type="checkbox"/>	Eukaryotic cell lines
<input checked="" type="checkbox"/>	<input type="checkbox"/>	Palaeontology and archaeology
<input type="checkbox"/>	<input checked="" type="checkbox"/>	Animals and other organisms
<input checked="" type="checkbox"/>	<input type="checkbox"/>	Clinical data
<input checked="" type="checkbox"/>	<input type="checkbox"/>	Dual use research of concern
<input checked="" type="checkbox"/>	<input type="checkbox"/>	Plants

## Methods

n/a	<input type="checkbox"/>	Involvement in the study
<input checked="" type="checkbox"/>	<input type="checkbox"/>	ChIP-seq
<input type="checkbox"/>	<input checked="" type="checkbox"/>	Flow cytometry
<input checked="" type="checkbox"/>	<input type="checkbox"/>	MRI-based neuroimaging

## Antibodies

## Antibodies used

Anti-human CD19-BB515 (Clone HIB19, BD Biosciences, #564456, lot 0016067)  
 Anti-human IgD-Pecy7 (Clone IA6-2, BD Biosciences, #561314, lot 1172562)  
 Anti-human CD27-BV421 (Clone M-T271 BD Biosciences, #562513, lot 1067357)  
 Anti-human CD86-PE (Clone IT2.2, BD Biosciences, #555665, lot 1104548)  
 Anti-human HLA-DR-AF700 (Clone G46-6, BD Biosciences, #560743, lot 1313902)  
 Anti-human CD24-BV711 (Clone ML5, BD Biosciences, #563401, lot 1214405)  
 Anti-human CD38-APC (Clone HIT2, BD Biosciences, #555462, lot 1270277)  
 Anti-human CD3 antibodies (Clone OKT-3, BioXCell, #BE0001-2)  
 anti-human CD28 antibodies (Clone 9.3, BioXCell, #BE0248)

## Validation

Antibodies were validated by manufacturer BD Biosciences. BD Biosciences' statement on antibody specificity validation: "The specificity is confirmed using multiple methodologies that may include a combination of flow cytometry, immunofluorescence, immunohistochemistry or western blot to test staining on a combination of primary cells, cell lines or transfectant models. All flow cytometry reagents are titrated on the relevant positive or negative cells. To save time and cell samples for researchers, test size reagents are bottled at an optimal concentration with the best signal-to-noise ratio on relevant models during the product development. To ensure consistent performance from lot-to-lot, each reagent is bottled to match the previous lot MFI.

## Eukaryotic cell lines

Policy information about [cell lines and Sex and Gender in Research](#)

## Cell line source(s)

L1210 cells were obtained from ATCC (Cat# CCL-219), THP-1 cells were graciously donated by the Chen lab at MIT (original source unknown), BaF-3 cells were obtained from RIKEN BioResource Center (Cat#RCB4476), FL5.12 cells were previously donated by the Vander Heiden lab at MIT (original source unknown). s-HeLa cells were previously donated by the Elias lab at Brigham and Women's Hospital (original source unknown). HL60 cells were previously donated by Thiam lab at Stanford (original source unknown). Patu-8902 cells were previously donated by the Hahn lab at the Broad Institute (original source unknown).

## Authentication

L1210 and BaF3 cell lines were authenticated by visual inspection of morphology. S-Hela and Patu-8902 cells were authenticated by visual inspection. HL60 cells were authenticated functionally by differentiating with DMSO and successfully inducing netosis. FL5.12 cells were authenticated functionally by culturing with and without IL-3 and confirming IL-3 dependent cell growth. No authentication tests were performed on other cell lines used in this study, including THP-1.

## Mycoplasma contamination

L1210 and BAF3 cell lines were tested for mycoplasma regularly. Other cell lines not tested.

Commonly misidentified lines  
(See [ICLAC](#) register)

No commonly misidentified cell lines were used.

## Animals and other research organisms

Policy information about [studies involving animals; ARRIVE guidelines](#) recommended for reporting animal research, and [Sex and Gender in Research](#)

## Laboratory animals

Athymic nude mice 6-12 wks old female. Mice are housed in the state of the art animal care facility at the Dana-Farber Cancer Institute with housing environment regulated for a 12 hour simulated light/dark cycle, Temperatures of 65-75°F (~18-23°C) with 40-60% humidity.

## Wild animals

The study did not involve using wild animals.

## Reporting on sex

Female mice were selected.

## Field-collected samples

The study did not involve using field-collected samples

## Ethics oversight

Dana-Farber Cancer Institute Institutional Care and Use Committee (DFCI-IACUC)

Note that full information on the approval of the study protocol must also be provided in the manuscript.

## Plants

Seed stocks	<input type="text" value="This study did not involve plants."/>
Novel plant genotypes	<input type="text" value="See above"/>
Authentication	<input type="text" value="See above"/>

## Flow Cytometry

### Plots

Confirm that:

- The axis labels state the marker and fluorochrome used (e.g. CD4-FITC).
- The axis scales are clearly visible. Include numbers along axes only for bottom left plot of group (a 'group' is an analysis of identical markers).
- All plots are contour plots with outliers or pseudocolor plots.
- A numerical value for number of cells or percentage (with statistics) is provided.

### Methodology

Sample preparation	<input type="text" value="Apheresis leukoreduction collars from three anonymous healthy platelet donors were obtained from the Brigham and Women's Hospital Specimen Bank under an Institutional Review Board-exempt protocol. Human peripheral blood mononuclear cells (PBMCs) were isolated with Ficoll-Paque Plus (Thermo Fisher Scientific, # 45001749) using the manufacturer's recommended protocol. The PBMC layer was isolated, subjected to ACK lysis (Life Technologies, # A1049201), and washed with PBS. Naïve B cells were isolated using EasySep™ Human Naïve B Cell Isolation Kit (Stem Cell, #17254) according to the Manufacturer's protocol. The Naïve B cells were seeded at 100,000-250,000 cells/mL in a 6-well plate and cultivated in the ImmunoCult™ Human B Cell Expansion Kit (Stem Cell, #100-0645). Unstimulated and stimulated naïve B cells were stained in Brilliant Stain Buffer for 20min at room temperature, washed with PBS supplemented with 2% FBS and 0.2% EDTA and analyze for flow cytometry."/>
Instrument	<input type="text" value="BD LSR Fortessa flow cytometer (BD Biosciences)"/>
Software	<input type="text" value="Data were acquired using BD FACSDiva Software and analyzed using FlowJo v10 software."/>
Cell population abundance	<input type="text" value="Approximately 10,000 cells gated on forward and side scatters were acquired for each sample. The less abundant cell population was 0.9% of the total event in the unstimulated cells."/>
Gating strategy	<input type="text" value="Cells were first gated based on forward and side scatters. FSC-W vs FSC-H and SS-W vs SSC-H were used to exclude doublets. Live cells were gated on Zombie Aqua negative cells. Lymphocytes were gated on CD19+. Naïve B cells were gated using CD19+/IgD+/CD27-/HLA-DR+/CD86-/CD38-, and activated naïve B cells using CD19+/IgD+/CD27-/HLA-DR+/CD86+/CD38-."/>

- Tick this box to confirm that a figure exemplifying the gating strategy is provided in the Supplementary Information.